

# Photo-neutron reaction cross-sections for $^{nat}\text{Zr}$ in the bremsstrahlung end-point energies of 12–16 and 45–70 MeV

H. Naik<sup>1</sup>, G.N. Kim<sup>2,a</sup>, R. Schwengner<sup>3</sup>, K. Kim<sup>2</sup>, M. Zaman<sup>2</sup>, S.C. Yang<sup>2</sup>, M.W. Lee<sup>2</sup>, S.G. Shin<sup>4</sup>, Y. Gey<sup>4</sup>, R. Massarczyk<sup>3</sup>, R. John<sup>3</sup>, A. Junghans<sup>3</sup>, A. Wagner<sup>3</sup>, A. Goswami<sup>1</sup>, and M.-H. Cho<sup>4</sup>

<sup>1</sup> Radiochemistry Division, Bhabha Atomic Research Centre, Mumbai 400085, India

<sup>2</sup> Department of Physics, Kyungpook National University, Daegu702-701, Republic of Korea

<sup>3</sup> Institute of Radiation Physics, Helmholtz-Zentrum Dresden-Rossendorf, 01328 Dresden, Germany

<sup>4</sup> Division of Advanced Nuclear Engineering, Pohang University of Science and Technology, Pohang 790-784, Republic of Korea

Received: 12 October 2013 / Revised: 30 January 2014

Published online: 9 May 2014 – © Società Italiana di Fisica / Springer-Verlag 2014

Communicated by P. Woods

**Abstract.** The  $^{nat}\text{Zr}(\gamma, xn)^{89-86}\text{Zr}$  reaction cross-sections were experimentally determined at the bremsstrahlung end-point energies of 12, 14, 16, 45, 50, 55, 60 and 70 MeV by activation and off-line  $\gamma$ -ray spectrometric technique using the 20 MeV electron linac (ELBE) at the Helmholtz-Zentrum Dresden-Rossendorf (HZDR), Dresden, Germany, and the 100 MeV electron linac at the Pohang Accelerator Laboratory (PAL), Pohang, Korea. The  $^{nat}\text{Zr}(\gamma, xn)^{89-86}\text{Zr}$  reaction cross-sections as a function of photon energy were also calculated using the TALYS 1.4 computer code. The flux-weighted average cross-sections at the end-point energies of 12–16 and 45–70 MeV were obtained using the literature and the TALYS calculation data based on mono-energetic photons and are found to be in good agreement with the present data. It was also found that the present data and the flux-weighted literature and theoretical values for the  $^{nat}\text{Zr}(\gamma, xn)^{89-86}\text{Zr}$  reaction cross-sections increase from the threshold values to a certain energy, where other reaction channels open. This indicates the role of excitation energy. However, the increasing trend of the  $^{nat}\text{Zr}(\gamma, xn)^{89,88}\text{Zr}$  reaction cross-sections are sharper from the threshold value up to end-point bremsstrahlung energies of 17–22 MeV compared to the same for the  $^{nat}\text{Zr}(\gamma, xn)^{87,86}\text{Zr}$  reactions. This is due to the Giant Dipole Resonance (GDR) effect besides the role of excitation energy. After a certain value, the individual  $^{nat}\text{Zr}(\gamma, xn)$  reaction cross-sections decrease with the increase of bremsstrahlung energy due to opening of other reactions, which indicates partitioning of energy in different channels.

## 1 Introduction

In the recent age, accelerator-driven sub-critical systems (ADSs) [1–6] are of primary interest for scientists to solve the problem of radiotoxic nuclear waste using transmutation of long-lived fission products and incineration of long-lived minor actinides, which were generated from the conventional nuclear reactors. The conversion of long-lived minor actinides and fission products into shorter-lived fission and reaction products [7], inside the sub-critical core of the ADSs, can be achieved by using an external neutron source. In ADSs, the high-energy neutrons with sufficient flux can be obtained from the spallation reaction, when GeV energy protons from an accelerator strike a heavy element like W, Pb, Bi, Th and U. Thus the spallation target becomes a source of neutrons, which drives a self-sustaining fission chain in a sub-critical core. In

the spallation processes, along with high-energy neutrons, high-energy photons are also produced, which can cause different types of nuclear reactions of the spallation target and cladding material. Among the different types of nuclear reactions, photo-neutron emission is one of the exit channels. The photo-neutrons can add to the neutron flux resulting from spallation, which can cause an increase of the total neutron flux. Thus, it is important to measure the photo-neutron cross-sections in the high-energy photon-induced reactions of the spallation target and cladding material. Among the different cladding materials, Zr and its alloy are the best for the ADSs and conventional nuclear reactors such as light-water reactors (BWR and PWR), heavy-water reactors (HWR) and advanced heavy-water reactors (AHWR).

Zirconium is a very strong malleable, ductile, lustrous, grayish-white metal and is highly resistant to corrosion by alkalis, acids, salt water and the other chemical agents. The high resistance to corrosion in aggressive

<sup>a</sup> e-mail: gnkim@knu.ac.kr

environments at high temperatures makes Zr metal appropriate in many applications, such as heat exchangers, pumps, reactor vessels, valves, surgical appliances and chemical industry, where corrosive agents are employed [8]. Although high-purity zirconium has very good corrosion resistance in water, it has low strength at high temperatures and thus alloying is required. Zr-based alloys containing Sn, Fe and Cr with or without Ni are called Zircaloy-2 and Zircaloy-4. Zircaloy-2 contains 1.5% tin, 0.1% iron, 0.1% chromium, 0.05% nickel, and no more than 0.01% nitrogen. Zircaloy-4 differs from Zircaloy-2 by lower nickel content (0.007%). The four alloying elements have negligible absorption cross-sections compared to the main (Zr) component of the alloy for low-energy neutrons. So they do not affect the neutron economy of the reactor, but allow the zirconium alloy to meet the required engineering criteria for cladding and assembly components. The Zr metal itself has a low neutron absorption cross-section [9–12] for low-energy neutrons. Therefore the nuclear power industry has the major application of the Zr and its alloy as the structural and cladding materials in ADSs and most of the conventional water reactors as mentioned above [13,14]. Zircaloy-2 is used in boiling-water reactors (BWR) and Zircaloy-4 in pressurized-water reactor (PWR). In pressurized heavy-water reactors (PHWR), Zr-2.5wt% Nb alloy is used as pressure tubes [15–17]. In the design of ADSs, ZrN is planned to be utilized as a main constituent of the nuclear fuel pellet.

From the above-mentioned points, it is clear that Zr and its alloys are important structural materials in conventional reactors and ADSs besides many other applications. Thus it is important to measure its medium-energy photon-, proton- and neutron-induced reactions cross-sections. Such data of the nuclear reactions of Zr are important for the design of conventional reactors and ADSs. The cross-sections data induced by different energy photons are also required for several other applications in the areas of applied nuclear physics, nuclear models and elemental analysis [18]. Sufficient data on  $(\gamma, n)$  and  $(\gamma, 2n)$  reaction cross-sections of  $^{90}\text{Zr}$  in the GDR region based on mono-energetic photons and using activation technique are reported in EXFOR compilation [19] from the work of various authors [20–28]. However, in the conventional reactor and ADSs, the photons produced are bremsstrahlung over a wide range of energies. Thus instead of mono-energetic photon, the bremsstrahlung-induced reaction cross-section of  $^{\text{nat}}\text{Zr}$  is of primary interest for ADSs design. In the literature, there is no data available on the  $^{\text{nat}}\text{Zr}(\gamma, xn)$  reaction cross-section for bremsstrahlung energy, except for the data at 10, 12.5 and 32 MeV [29,30]. In view of this, in the present work, the  $^{\text{nat}}\text{Zr}(\gamma, xn)^{89-86}\text{Zr}$  reaction cross-sections at the bremsstrahlung end-point energies of 12–16 and 45–70 MeV have been determined by using an activation and off-line  $\gamma$ -ray spectrometric technique. The  $^{\text{nat}}\text{Zr}(\gamma, xn)^{89-86}\text{Zr}$  reaction cross-sections at different bremsstrahlung end-point energies were also calculated using the TALYS 1.4 code [31] and the results were compared with the experimental values of the present work.

## 2 Experimental details

The experiments were performed by using the 20 MeV electron linac (ELBE) at the Helmholtz-Zentrum Dresden-Rossendorf (HZDR), Dresden, Germany, and the 100 MeV electron linac at the Pohang accelerator laboratory (PAL), Pohang, Korea. The 20 MeV electron linac was used for the bremsstrahlung end-point energies of 12, 14 and 16 MeV, whereas the 100 MeV electron linac for the 45, 50, 55, 60 and 70 MeV, respectively.

In the 20 MeV electron linac, irradiations were done for the measurement of the  $^{90}\text{Zr}(\gamma, n)^{89}\text{Zr}$  reaction cross-section at the bremsstrahlung end-point energy of 16 MeV and for the  $^{96}\text{Zr}(\gamma, n)^{95}\text{Zr}$  reaction at 12, 14 and 16 MeV, respectively. For each irradiation, a stack of  $^{\text{nat}}\text{Zr}$ -Au sample was made. The size of the high-purity (99.999%)  $^{\text{nat}}\text{Zr}$  metal foil was  $1\text{ cm} \times 0.7\text{--}0.8\text{ cm}$  with thickness of 0.1 mm and weight 54.4 to 63.6 mg. On the other hand, the size of the Au metal foil was  $0.8\text{ cm} \times 0.7\text{--}0.6\text{ cm}$  with thickness 0.1 mm and weight 83.2 to 101.6 mg. The  $^{197}\text{Au}(\gamma, n)^{196}\text{Au}$  reaction was used as the photon flux monitor. All samples were wrapped individually with 0.025 mm thick super pure aluminum foil with purity higher than 99.99%. The three different sets of samples were kept inside separate capsules made of polypropylene. They were loaded on a sample holder and then sent one at a time to the place of irradiation using a pneumatic carrier rabbit facility [32,33]. The bremsstrahlung radiation was generated by impinging the electron beam on a solid graphite beam dump [32,33]. The area directly behind the electron beam dump was used as a site for high flux ( $\sim 10^9$  to  $10^{10}$  photons  $\text{cm}^{-2} \text{s}^{-1}$ ) irradiations. Then individual sample irradiations were done for 8.5 to 10.5 hours with the bremsstrahlung end-point energies of 12, 14 and 16 MeV, respectively. During the experiments, the electron LINAC was operated with a pulse repetition rate (PRR) of 13 MHz, a pulse width of 10 picoseconds and an average beam current of 550  $\mu\text{A}$ . The electron beam current was very much stable during the irradiation time of 8.5–10.5 h. Thus it produces constant photon flux throughout the irradiation. After the irradiation, the samples were brought back to the detector by using the same automated pneumatic rabbit carrier facility. Then, the  $\gamma$ -ray counting of the irradiated targets of  $^{\text{nat}}\text{Zr}$  and Au along with an aluminum catcher was done by using an energy- and efficiency-calibrated 90% HPGe detector coupled to a PC-based 16 K channel analyzer. The resolution of the detector system was 2.0 keV at 1332.0 keV of  $^{60}\text{Co}$ . The sample was kept at a suitable distance from the detector to optimize the count rate and the dead time. At the same time the dead time of the detector system was kept below 10% to avoid the coincidence and summing effects. The energy and efficiency calibration of the detector system was done by counting the  $\gamma$ -ray energies of standard sources such as  $^{133}\text{Ba}$ ,  $^{137}\text{Cs}$ ,  $^{22}\text{Na}$  and  $^{60}\text{Co}$ .

In the case of the 100 MeV electron linac, different irradiations were done at bremsstrahlung end-point energies of 45, 50, 55, 60 and 70 MeV to measure the  $(\gamma, xn)$  reactions cross-sections of  $^{\text{nat}}\text{Zr}$ . The bremsstrahlung was generated when a pulsed electron beam hit a thin tungsten

(W) metal foil with a size of 10.0 cm × 10.0 cm and a thickness of 0.1 mm [34]. The W target was placed on a suitable stand at 18.0 cm from the electron beam exit window. The  $^{nat}\text{Zr}$  metal foil with an area of 1.0 cm × 1.0 cm and weight of 71.6 to 75.3 mg was wrapped with a 0.025 mm thick Al foil. Similarly, the Au metal foil of same size was also wrapped with 0.025 mm thick Al foil. The Al wrapper is necessary to stop reaction products recoiling out from the target during irradiation and to avoid radioactive contamination to the surrounding. Then a stack of  $^{nat}\text{Zr}$ -Au sample was made, which was additionally wrapped with one more Al foil. The  $^{197}\text{Au}(\gamma, n)^{196}\text{Au}$  reaction was used as the photon flux monitor for the  $^{96}\text{Zr}(\gamma, n)^{95}\text{Zr}$  and  $^{nat}\text{Zr}(\gamma, xn)^{89}\text{Zr}$  reactions. On the other hand, the  $^{27}\text{Al}(\gamma, 2pn)^{24}\text{Na}$  reaction of the Al wrapper was used to determine the photon flux for the  $^{nat}\text{Zr}(\gamma, xn)^{88}\text{Zr}$ , and  $^{nat}\text{Zr}(\gamma, xn)^{87}\text{Zr}$  and  $^{nat}\text{Zr}(\gamma, xn)^{86}\text{Zr}$  reactions. The uses of different detectors for various reactions are based on their threshold values. The target stack assembly was fixed on a stand at a proper height behind the 0.1 mm thick W metal foil [34]. The sample was placed at 12 cm from the W target and was positioned at zero degree with respect to the direction of the electron beam. Different sets of targets for Zr-Au stack were made for different irradiations. The target assembly was irradiated for 0.5–3 h with bremsstrahlung produced by bombarding the 45–70 MeV electrons on the tungsten metal foil. The current of the electron beam during irradiation was 10–35 mA at 3.75 Hz with a beam width of 1.5  $\mu\text{s}$ . The electron beam current was very much stable during the irradiation time of 0.5–3 h. Thus it produces constant photon flux throughout the irradiation. However, during the irradiation some electrons also produce or pass through the thin tungsten along with the bremsstrahlung. Within the Weizsäcker-Williams approximation [35,36], the electron-nucleus interaction occurs through a spectrum of virtual photons, whereas the bremsstrahlung is composed of real photons. Thus, the photo-nuclear reactions at the high-energy electron beam are due to the spectrum of bremsstrahlung and virtual photons. After the irradiation, the irradiated target was kept for 3–30 min to cool down. Then the cooled irradiated targets of Zr and Au along with individual Al wrapper were taken out from the irradiated assembly and mounted separately on different Perspex (acrylic glass, 1.5 mm thick) plates [34]. The  $\gamma$ -ray counting of the reaction products from  $^{nat}\text{Zr}$ ,  $^{197}\text{Au}$  and  $^{27}\text{Al}$  was done by using an energy- and efficiency-calibrated HPGe detector coupled to a PC-based 4K channel analyzer. The resolution of the detector system had a full width at half maximum (FWHM) of 1.8 keV at the 1332.5 keV peak of  $^{60}\text{Co}$ . The standard source used for the energy and the efficiency calibration was  $^{152}\text{Eu}$ , having  $\gamma$ -rays in the energy range of 121.8–1408.0 keV. The detector efficiency was 20% at 1332.5 keV relative to a 7.6 cm diameter × 7.6 cm length NaI(Tl) detector. The dead time of the detector system during counting was always kept less than 10% to avoid pileup effects. The  $\gamma$ -ray counting of the reaction products from the irradiated samples of  $^{nat}\text{Zr}$ ,  $^{197}\text{Au}$  and  $^{27}\text{Al}$  was done by placing the samples in the shelf, which was 5 cm

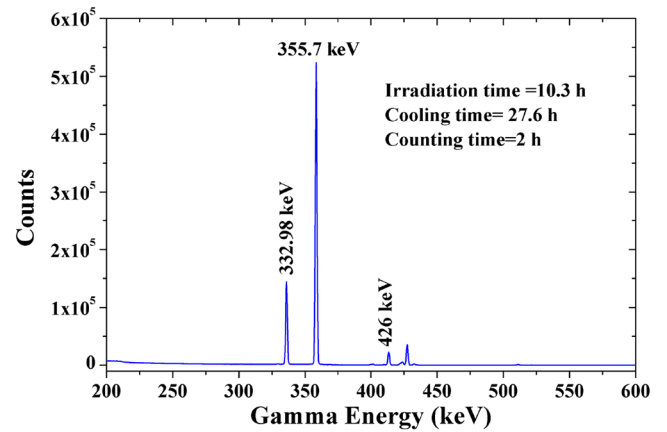


**Fig. 1.** Typical  $\gamma$ -ray spectrum of an irradiated gold foil with bremsstrahlung end-point energy of 16 MeV.

away from the detector. The  $\gamma$ -ray counting of the sample was done in live time mode and was followed as a function of time for at least three half-lives. Typical  $\gamma$ -ray spectra of the irradiated  $^{197}\text{Au}$  and  $^{nat}\text{Zr}$  samples along with  $^{27}\text{Al}$  wrapper from the irradiation of bremsstrahlung end-point energies of 16 MeV from ELBE and 55 MeV from PAL electron linac are given in figs. 1 and 2, respectively.

## 3 Data analysis

### 3.1 Calculation of photon flux

The net peak area ( $A_{\text{net}}$ ) corresponding to the photo-peak was calculated by summing the counts under the full energy peak and subtracting the linear Compton background. In the case of the 12–16 MeV bremsstrahlung irradiation, the photon flux was determined based on the activities of 332.98, 355.7 and 426.0 keV  $\gamma$ -rays of  $^{196}\text{Au}$  from the  $^{197}\text{Au}(\gamma, n)$  reaction. On the other hand, in the case of the 45–70 MeV bremsstrahlung irradiation, the photon flux was determined based on the activities of 332.98, 355.7 and 426.0 keV  $\gamma$ -rays of  $^{196}\text{Au}$  from the  $^{197}\text{Au}(\gamma, n)$  reaction as well as the activity of 1368.6 keV  $\gamma$ -ray of  $^{24}\text{Na}$  from the  $^{27}\text{Al}(\gamma, 2pn)$  reaction. The photo-peak activities ( $A_{\text{net}}$ ) for the  $\gamma$ -rays of  $^{196}\text{Au}$  and  $^{24}\text{Na}$  are related to the photon flux ( $\varphi$ ) by the equation

$$A_{\text{(net)}} \left( \frac{CL}{LT} \right) = \frac{N \langle \sigma \rangle \Phi a \varepsilon (1 - e^{-\lambda t}) (e^{-\lambda T}) (1 - e^{-\lambda CL})}{\lambda}, \quad (1)$$

where  $N$  is the number of target atoms and  $\langle \sigma \rangle$  the average activation cross-section of the  $^{197}\text{Au}(\gamma, n)^{196}\text{Au}$  and  $^{27}\text{Al}(\gamma, 2pn)^{24}\text{Na}$  reactions.  $\Phi = \int_{E_{\text{th}}}^{E_e} \varphi$  is the bremsstrahlung flux with photon flux  $\varphi$  from the threshold value ( $E_{\text{th}}$ ) to the end-point bremsstrahlung energy ( $E_e$ ) [34]; “ $a$ ” the absolute  $\gamma$ -ray emission probability of the analyzed  $\gamma$ -rays and  $\varepsilon$  the detection efficiency of the activated product; “ $t$ ”,  $T$ ,  $CL$  and  $LT$  are the irradiation, cooling, real and live time, respectively; “ $\lambda$ ” is the decay constant ( $= \ln 2/T_{1/2}$ ) for the isotope of interest.

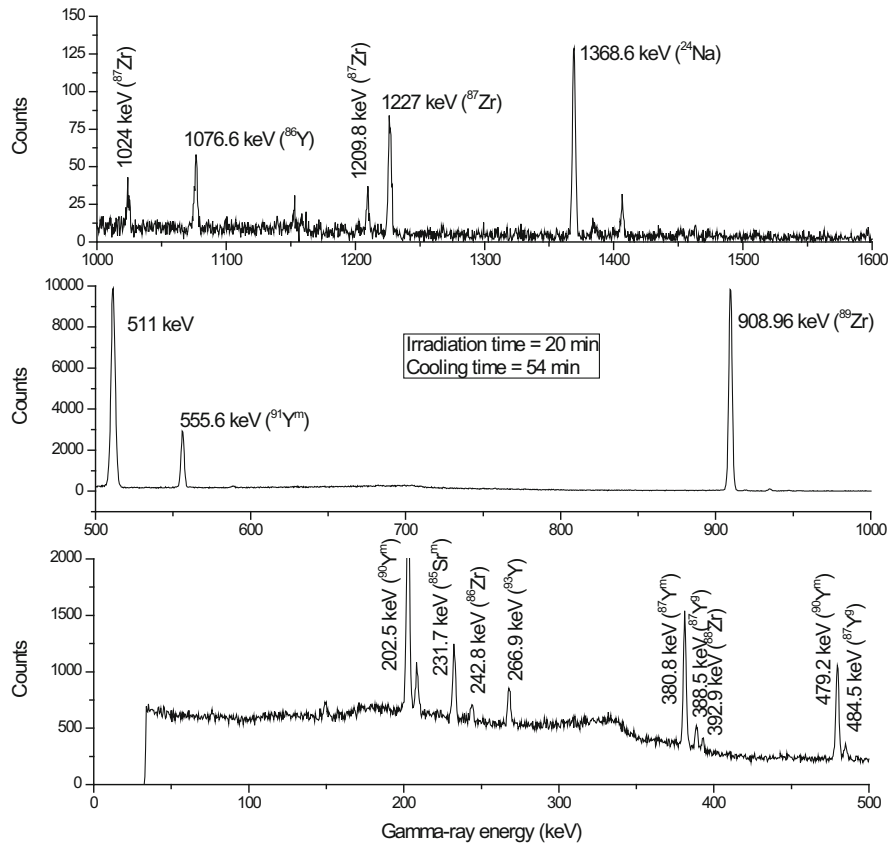


**Fig. 2.** Typical  $\gamma$ -ray spectrum of an irradiated  $^{nat}\text{Zr}$  along with  $^{27}\text{Al}$  wrapper with bremsstrahlung end-point energy of 55 MeV showing the  $\gamma$ -lines of  $^{89}\text{Zr}$ ,  $^{88}\text{Zr}$ ,  $^{87}\text{Zr}$ ,  $^{86}\text{Zr}$  from the  $^{nat}\text{Zr}(\gamma, xn)$  reaction,  $^{85}\text{mSr}$ ,  $^{86}\text{Y}$ ,  $^{87\text{m,g}}\text{Y}$ ,  $^{90\text{m}}\text{Y}$  and  $^{91\text{m}}\text{Y}$  from the  $^{nat}\text{Zr}(\gamma, x)$  reaction and  $^{24}\text{Na}$  from the  $^{27}\text{Al}(\gamma, 2pn)$  reaction, respectively.

In the above equation, the peak area has been corrected for the dead time by multiplying with the  $CL/LT$  factor. The  $\gamma$ -ray energies and the decay data for the residual nuclide such as branching ratio, half-lives are taken from refs. [37,38] and given in table 1. In the case of 12–16 MeV bremsstrahlung irradiations, the average cross-section ( $\langle\sigma\rangle$ ) for  $^{197}\text{Au}(\gamma, n)^{196}\text{Au}$  reaction was calculated using the following relation:

$$\langle\sigma\rangle = \frac{\sum \sigma \varphi}{\sum \varphi}. \quad (2)$$

The photon flux distributions for the bremsstrahlung end-point energies of 12, 14 and 16 MeV were calculated by using the GEANT4 code [39,40]. The photon flux ( $\varphi$ ) distribution with respect to photon energy ( $E$ ) is presented in fig. 3. Photo nuclear cross-section ( $\sigma$ ) of  $^{197}\text{Au}(\gamma, n)^{196}\text{Au}$  reaction has been reported by many groups [41–44]. For our calculation, we have used the  $\sigma$  value from ref. [45] for mono-energetic photons, which is shown in fig. 4 along with the calculated values of the TALYS 1.4 [31] computer code. A short description of the TALYS 1.4 computer code is given in the next section. It can be seen, from fig. 4, that TALYS calculation describes well the experimental  $^{197}\text{Au}(\gamma, n)^{196}\text{Au}$  reaction cross-section ( $\sigma$ ) data based on mono-energetic photons [45]. Thus it is acceptable

to use the extrapolation and interpolation of the experimental data based on calculated values of TALYS. For the bremsstrahlung end-point energy of the present work, the TALYS cross-section based on mono-energetic photon was folded with the photon flux to calculate the average  $^{197}\text{Au}(\gamma, n)^{196}\text{Au}$  reaction cross-section ( $\langle\sigma\rangle$ ) and shown in table 2. Then, the bremsstrahlung flux ( $\Phi$ ) for the  $^{197}\text{Au}(\gamma, n)^{196}\text{Au}$  reaction was calculated using the flux-weighted cross-section value ( $\langle\sigma\rangle$ ) in eq. (1) and by rearranging the terms. The threshold ( $E_{\text{th}}$ ) for the  $^{197}\text{Au}(\gamma, n)^{196}\text{Au}$ ,  $^{96}\text{Zr}(\gamma, n)^{95}\text{Zr}$  and  $^{90}\text{Zr}(\gamma, n)^{89}\text{Zr}$  reactions are 8.073, 7.856 and 11.97 MeV, respectively. Thus the photon flux obtained from the  $^{197}\text{Au}(\gamma, n)^{196}\text{Au}$  reaction has to be modified for the  $^{96}\text{Zr}(\gamma, n)^{95}\text{Zr}$  and  $^{90}\text{Zr}(\gamma, n)^{89}\text{Zr}$  reactions based on threshold value ( $E_{\text{th}}$ ) to bremsstrahlung end-point energy ( $E_e$ ). In case of the  $^{96}\text{Zr}(\gamma, n)^{95}\text{Zr}$  reaction at bremsstrahlung end-point energies ( $E_e$ ) of 12, 14 and 16 MeV, the weighted average flux obtained from the  $^{197}\text{Au}(\gamma, n)^{196}\text{Au}$  reaction is multiplied by factors of 1.078, 1.059 and 1.047, respectively. These factors are the flux ratios for the  $^{96}\text{Zr}(\gamma, n)^{95}\text{Zr}$  reaction from 7.856 MeV to 12, 14 and 16 MeV divided by the  $^{197}\text{Au}(\gamma, n)^{196}\text{Au}$  reaction from 8.073 MeV to 12, 14 and 16 MeV, respectively. As an example the calculation of flux conversion ratio (factor) at the end-point bremsstrahlung energy of

**Table 1.** Nuclear spectroscopic data of the radio-nuclides from the  $^{197}\text{Au}(\gamma, n)^{196}\text{Au}$ ,  $^{27}\text{Al}(\gamma, 2pn)^{24}\text{Na}$ ,  $^{96}\text{Zr}(\gamma, n)^{95}\text{Zr}$ ,  $^{\text{nat}}\text{Zr}(\gamma, xn)^{89\text{m,g}}\text{Zr}$ ,  $^{\text{nat}}\text{Zr}(\gamma, xn)^{88}\text{Zr}$ ,  $^{\text{nat}}\text{Zr}(\gamma, xn)^{87}\text{Zr}$  and  $^{\text{nat}}\text{Zr}(\gamma, xn)^{86}\text{Zr}$  reactions [37,38].

| Nuclide                  | Half-life | Decay mode (%)                      | $\gamma$ -ray energy (keV) <sup>(a)</sup> | Absolute decay probability (%) | Reactions                     | Q-value (MeV) | Threshold (MeV) |
|--------------------------|-----------|-------------------------------------|---|--------------------------------|-------------------------------|---------------|-----------------|
| $^{196}\text{Au}$        | 6.183 d   | $\beta^+$ (92.8)<br>$\beta^-$ (7.2) | 332.983                                   | 22.9                           | $^{197}\text{Au}(\gamma, n)$  | -8.072        | 8.073           |
|                          |           |                                     | <b>355.689</b>                            | 87                             |                               |               |                 |
|                          |           |                                     | 426.0                                     | 7                              |                               |               |                 |
| $^{24}\text{Na}$         | 14.959 h  | $\beta^-$ (100)                     | <b>1368.6</b>                             | 100                            | $^{27}\text{Al}(\gamma, 2pn)$ | -31.428       | 31.447          |
|                          |           |                                     | 2754.028                                  | 99.944                         |                               |               |                 |
| $^{95}\text{Zr}$         | 64.02 d   | $\beta^-$ (100)                     | <b>724.2</b>                              | 44.17                          | $^{96}\text{Zr}(\gamma, n)$   | 7.856         | 7.857           |
|                          |           |                                     | <b>756.7</b>                              | 54                             |                               |               |                 |
| $^{89\text{m}}\text{Zr}$ | 4.18 m    | $\beta^+$ (6.23)<br>IT(93.77)       | <b>587.83</b><br><b>1507.11</b>           | 90                             | $^{90}\text{Zr}(\gamma, n)$   | -11.970       | 11.971          |
|                          |           |                                     |   | 6.06                           | $^{91}\text{Zr}(\gamma, 2n)$  | -19.164       | 19.166          |
|                          |           |                                     |   |                                | $^{92}\text{Zr}(\gamma, 3n)$  | -27.799       | 27.803          |
|                          |           |                                     |   |                                | $^{94}\text{Zr}(\gamma, 5n)$  | -42.755       | 42.765          |
| $^{89\text{g}}\text{Zr}$ | 78.41 h   | $\beta^+$ (100)                     | <b>908.96</b>                             | 100                            | $^{90}\text{Zr}(\gamma, n)$   | -11.970       | 11.971          |
|                          |           |                                     |   |                                | $^{91}\text{Zr}(\gamma, 2n)$  | -19.164       | 19.166          |
|                          |           |                                     |   |                                | $^{92}\text{Zr}(\gamma, 3n)$  | -27.799       | 27.803          |
|                          |           |                                     |   |                                | $^{94}\text{Zr}(\gamma, 5n)$  | -42.755       | 42.765          |
| $^{88}\text{Zr}$         | 83.4 d    | EC (100)                            | <b>392.87</b>                             | 100                            | $^{90}\text{Zr}(\gamma, 2n)$  | -21.286       | 21.289          |
|                          |           |                                     |   |                                | $^{91}\text{Zr}(\gamma, 3n)$  | -28.481       | 28.486          |
|                          |           |                                     |   |                                | $^{92}\text{Zr}(\gamma, 4n)$  | -37.116       | 37.124          |
|                          |           |                                     |   |                                | $^{94}\text{Zr}(\gamma, 6n)$  | -52.071       | 52.087          |
| $^{87}\text{Zr}$         | 1.68 h    | $\beta^+$ (100)                     | <b>1227.0</b>                             | 1                              | $^{90}\text{Zr}(\gamma, 3n)$  | -33.633       | 33.640          |
|                          |           |                                     |   |                                | $^{91}\text{Zr}(\gamma, 4n)$  | -40.828       | 40.837          |
|                          |           |                                     |   |                                | $^{92}\text{Zr}(\gamma, 5n)$  | -49.462       | 49.477          |
| $^{86}\text{Zr}$         | 16.5 h    | $\beta^+$ (100)                     | <b>242.8</b><br>1198.4                    | 45                             | $^{90}\text{Zr}(\gamma, 4n)$  | -43.248       | 43.259          |
|                          |           |                                     |   | 4.8                            | $^{91}\text{Zr}(\gamma, 5n)$  | -50.442       | 50.457          |
|                          |           |                                     |   |                                | $^{92}\text{Zr}(\gamma, 6n)$  | -59.077       | 59.097          |

(a) The bold numbers are the  $\gamma$ -ray energies, whose activities were used in the calculation.

$E_e$  for the  $^{96}\text{Zr}(\gamma, n)^{95}\text{Zr}$  reaction following formula was used:

$$\text{Factor} = \int_{E_{\text{th-Zr}}}^{E_e} \varphi d\varphi / \int_{E_{\text{th-Au}}}^{E_e} \varphi d\varphi. \quad (3)$$

For this purpose the photon beam flux ( $\varphi$ ) distribution was simulated by the GEANT4 code [39,40] and used for the renormalization of the experimental flux based on the monitor  $^{197}\text{Au}(\gamma, n)^{196}\text{Au}$  reaction. In the case of the  $^{\text{nat}}\text{Zr}(\gamma, xn)^{89}\text{Zr}$  reaction at the bremsstrahlung end-point energy of 16 MeV, 100% reaction cross-sections come from the  $^{90}\text{Zr}(\gamma, n)^{89}\text{Zr}$  reaction due to the threshold value of 11.97 MeV. Thus the weighted average flux obtained from the  $^{197}\text{Au}(\gamma, n)^{196}\text{Au}$  reaction is multiplied by a factor of 0.313. This factor is the flux ratio for the  $^{90}\text{Zr}(\gamma, n)^{89}\text{Zr}$  reaction from 11.97 to 16 MeV divided by the  $^{197}\text{Au}(\gamma, n)^{196}\text{Au}$  reaction from 8.073 to 16 MeV. The different ratios used for the conversion of the photon flux

for the  $^{96}\text{Zr}(\gamma, n)^{95}\text{Zr}$  and  $^{90}\text{Zr}(\gamma, n)^{89}\text{Zr}$  reactions to the total flux of the  $^{197}\text{Au}(\gamma, n)^{196}\text{Au}$  reaction based on the threshold values for the bremsstrahlung end-point energies of 12, 14 and 16 MeV are given in table 2.

In the case of bremsstrahlung irradiations of 45–70 MeV, the photon flux distribution were also calculated by using the GEANT4 code [39,40]. The photon flux ( $\varphi$ ) distribution with respect to photon energy ( $E$ ) is presented in fig. 3. The bremsstrahlung flux ( $\Phi$ ) during an individual irradiation was obtained from the observed activities ( $A_{\text{net}}$ ) of the 332.98, 355.7, 426.0 and 1368.6 keV  $\gamma$ -lines of  $^{196}\text{Au}$  and  $^{24}\text{Na}$  produced from the  $^{197}\text{Au}(\gamma, n)$  and  $^{27}\text{Al}(\gamma, 2pn)$  reactions, respectively. For the  $^{197}\text{Au}(\gamma, n)^{196}\text{Au}$  reaction, the average cross-section ( $\langle\sigma\rangle$ ) for the  $^{197}\text{Au}(\gamma, n)^{196}\text{Au}$  reaction was calculated as mentioned before (eq. (2)) from the  $\sigma$  value of TALYS [31] for mono-energetic photons. This is because the flux-weighted reaction cross-section ( $\langle\sigma_R\rangle$ ) from

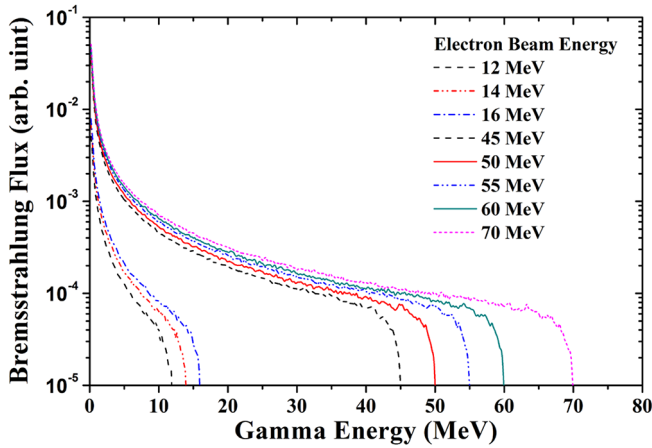


**Fig. 3.** Plot of bremsstrahlung spectrum for end-point energies of 12, 14, 16, 45, 50, 55, 60, and 70 MeV calculated by using the GEANT4 code [39,40].

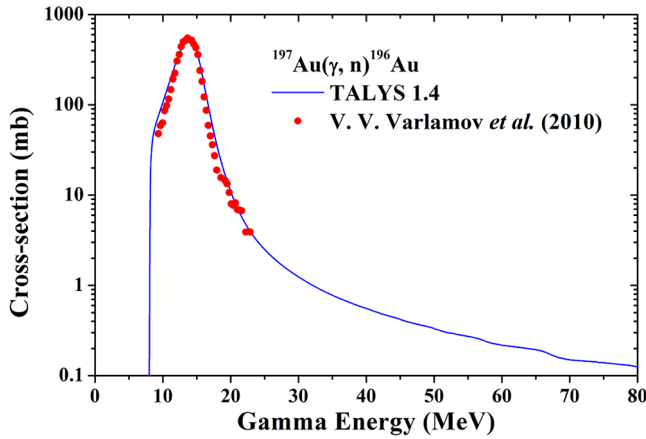


**Fig. 4.** Cross-sections of the  $^{197}\text{Au}(\gamma, n)^{196}\text{Au}$  reaction as a function of gamma-ray energy obtained from the experimental data [45] and the calculated values from the TALYS [31] based on the mono-energetic photons, which are shown with continuous lines.

ref. [45] can be obtained only up to the bremsstrahlung end-point energy of 24 MeV. On the other hand, the  $^{27}\text{Al}(\gamma, 2\text{pn})^{24}\text{Na}$  reaction, the  $\langle\sigma_R\rangle$  value in the range of 0.045–0.2 mb corresponding to the bremsstrahlung end-point energy range of 45–70 MeV is available in ref. [46] and thus was used in eq. (1) to obtain the bremsstrahlung flux ( $\Phi$ ). The threshold value for the  $^{27}\text{Al}(\gamma, 2\text{pn})^{24}\text{Na}$  reaction is 31.073 MeV. However,  $^{\text{nat}}\text{Zr}$  has many isotopes with isotopic composition of  $^{90}\text{Zr}$  (51.45%),  $^{91}\text{Zr}$  (11.22%),  $^{92}\text{Zr}$  (17.15%),  $^{94}\text{Zr}$  (17.38%) and  $^{96}\text{Zr}$  (2.80%), respectively. So for the production of the same reaction product from the reactions of different Zr isotopes, the threshold values are different. Similarly, for the different reaction products from the same isotope of Zr, the reactions thresholds are different. As an example, the threshold for the production cross-section of same product  $^{89}\text{Zr}$  from the reaction of different isotopes of Zr such as  $^{90}\text{Zr}(\gamma, n)^{89}\text{Zr}$ ,  $^{91}\text{Zr}(\gamma, 2n)^{89}\text{Zr}$ ,  $^{92}\text{Zr}(\gamma, 3n)^{89}\text{Zr}$

and  $^{94}\text{Zr}(\gamma, 5n)^{89}\text{Zr}$  reactions are 11.97, 19.17, 27.8 and 42.77 MeV, respectively. Similarly, the threshold values for different reaction products such as  $^{89}\text{Zr}$ ,  $^{88}\text{Zr}$ ,  $^{87}\text{Zr}$  and  $^{86}\text{Zr}$  from the  $^{90}\text{Zr}(\gamma, n)^{89}\text{Zr}$ ,  $^{90}\text{Zr}(\gamma, 2n)^{88}\text{Zr}$ ,  $^{90}\text{Zr}(\gamma, 3n)^{87}\text{Zr}$  and  $^{90}\text{Zr}(\gamma, 4n)^{86}\text{Zr}$  reactions are 11.97, 21.29, 33.64, 55.99 MeV, respectively. As described in the next section, more than 88–93% formation cross-sections of  $^{89}\text{Zr}$ ,  $^{88}\text{Zr}$ ,  $^{87}\text{Zr}$  and  $^{86}\text{Zr}$  comes from the  $(\gamma, n)$ ,  $(\gamma, 2n)$ ,  $(\gamma, 3n)$  and  $(\gamma, 4n)$  reaction of the 51.45% of  $^{90}\text{Zr}$  in the  $^{\text{nat}}\text{Zr}$ . Thus the photon flux obtained from the  $^{197}\text{Au}(\gamma, n)^{196}\text{Au}$  and  $^{27}\text{Al}(\gamma, n)^{24}\text{Na}$  reactions have to be modified for the  $(\gamma, n)$ ,  $(\gamma, 2n)$ ,  $(\gamma, 3n)$  and  $(\gamma, 4n)$  reactions of  $^{90}\text{Zr}$  based on the threshold values to the bremsstrahlung end-point energy as described in eq. (3). The photon flux conversion ratio (factor) for the  $(\gamma, n)$ ,  $(\gamma, 2n)$ ,  $(\gamma, 3n)$  and  $(\gamma, 4n)$  reactions of  $^{90}\text{Zr}$  to the  $^{27}\text{Al}(\gamma, n)^{24}\text{Na}$  reaction at the end-point bremsstrahlung energy of 45 MeV are 4.754, 2.372, 0.764 and 0.063, respectively. Similarly, in the case of the  $^{\text{nat}}\text{Zr}(\gamma, n)^{89}\text{Zr}$  reaction, the photon flux from the  $^{197}\text{Au}(\gamma, n)^{196}\text{Au}$  reaction was modified at the bremsstrahlung end-point energies of 45–70 MeV as in the case of 16 MeV. As an example, the flux conversion ratio for the  $(\gamma, n)$  reaction of  $^{90}\text{Zr}$  to the  $^{197}\text{Au}(\gamma, n)^{196}\text{Au}$  reaction at the end-point bremsstrahlung energies of 12, 14, 16, 45, 50, 55, 60 and 70 MeV are 0.005, 0.185, 0.313, 0.720, 0.735, 0.745, 0.753 and 0.822, respectively. On the other hand, the flux conversion ratio for the  $(\gamma, n)$  reaction of  $^{90}\text{Zr}$  to the  $^{27}\text{Al}(\gamma, n)^{24}\text{Na}$  reaction at the end-point bremsstrahlung energies of 45, 50, 55, 60 and 70 MeV are 4.754, 3.870, 3.368, 3.017 and 2.609, respectively. However, for the  $^{90}\text{Zr}(\gamma, n)^{89}\text{Zr}$  reaction, the flux conversion ratio based on the  $^{197}\text{Au}(\gamma, n)^{196}\text{Au}$  reaction has been used to obtain the bremsstrahlung flux. For the  $(\gamma, 2n)$ ,  $(\gamma, 3n)$  and  $(\gamma, 4n)$  reactions of  $^{90}\text{Zr}$  at the bremsstrahlung end-point energies of 45, 50, 55, 60 and 70 MeV, the weighted average flux obtained from the  $^{27}\text{Al}(\gamma, 2\text{pn})^{24}\text{Na}$  reaction is multiplied by different flux conversion ratios (factors), which are shown in table 2.

### 3.2 Calculation of the $^{\text{nat}}\text{Zr}(\gamma, xn)$ reaction cross-sections and their yield percentage

In the present work, the radio-nuclides observed from the  $^{\text{nat}}\text{Zr}(\gamma, xn)$  reactions are  $^{95}\text{Zr}$ ,  $^{89}\text{Zr}^{\text{m,g}}$ ,  $^{88}\text{Zr}$ ,  $^{87}\text{Zr}$  and  $^{86}\text{Zr}$  having different half-lives and  $\gamma$ -ray energies. The nuclear spectroscopic data for the reaction products from  $^{\text{nat}}\text{Zr}(\gamma, xn)$  reactions were taken from refs. [37,38] and shown in table 1. The net peak areas ( $A_{\text{net}}$ ) corresponding to the photo-peak for different reaction products were calculated by summing the counts under the full energy peak and subtracting the linear Compton background. From the net photo-peak area ( $A_{\text{net}}$ ) of the formation cross-sections of  $^{95}\text{Zr}$ ,  $^{89}\text{Zr}^{\text{m,g}}$ ,  $^{88}\text{Zr}$ ,  $^{87}\text{Zr}$  and  $^{86}\text{Zr}$  in the  $^{\text{nat}}\text{Zr}(\gamma, xn)$  reactions were obtained using the following equation [34]:

$$\sigma = \frac{A_{\text{net}} \left(\frac{CL}{LT}\right) \lambda}{N\Phi a \varepsilon (1 - e^{-\lambda t})(e^{-\lambda T})(1 - e^{-\lambda CL})}. \quad (4)$$

**Table 2.** Average cross-section ( $\langle\sigma\rangle$ ) for the  $^{197}\text{Au}(\gamma, n)^{196}\text{Au}$  and  $^{27}\text{Al}(\gamma, 2\text{pn})^{24}\text{Na}$  reactions. The flux conversion ratios (factors) used to obtain the photon flux for different reactions of  $^{\text{nat}}\text{Zr}$  from the total flux based on the  $^{197}\text{Au}(\gamma, n)^{196}\text{Au}$  and  $^{27}\text{Al}(\gamma, 2\text{pn})^{24}\text{Na}$  reactions flux monitors.

| Bremsstrahlung Energy (MeV)   | 12    | 14    | 16    | 45    | 50    | 55    | 60    | 70    |
|---|-------|-------|-------|-------|-------|-------|-------|-------|
| $\langle\sigma\rangle$ of $^{197}\text{Au}(\gamma, n)^{196}\text{Au}$ (mb)  | 98.92 | 173.0 | 221.4 | 118.5 | 113.0 | 106.3 | 101.8 | 95.74 |
| $\langle\sigma\rangle$ of $^{27}\text{Al}(\gamma, 2\text{pn})^{24}\text{Na}$ (mb)                                       | –     | –     | –     | 0.045 | 0.068 | 0.092 | 0.116 | 0.158 |
| $^{96}\text{Zr}(\gamma, n)/^{197}\text{Au}(\gamma, n)$<br><i>i.e.</i> $(7.9-E_\gamma)/(8.0-E_\gamma)$                   | 1.078 | 1.059 | 1.047 | 1.018 | 1.018 | 1.017 | 1.017 | 1.065 |
| $^{90}\text{Zr}(\gamma, n)/^{197}\text{Au}(\gamma, n)$<br><i>i.e.</i> $(7.9-E_\gamma)/(8.0-E_\gamma)$                   | 0.005 | 0.185 | 0.313 | 0.720 | 0.735 | 0.745 | 0.753 | 0.822 |
| $^{90}\text{Zr}(\gamma, n)/^{27}\text{Al}(\gamma, n)$<br><i>i.e.</i> $(11.97-E_\gamma)/(31.4-E_\gamma)$                 | –     | –     | –     | 4.754 | 3.870 | 3.368 | 3.017 | 2.609 |
| $^{91}\text{Zr}(\gamma, 2\text{n})/^{27}\text{Al}(\gamma, n)$<br><i>i.e.</i> $(19.2-E_\gamma)/(31.4-E_\gamma)$          | –     | –     | –     | 2.769 | 2.348 | 2.143 | 1.980 | 1.785 |
| $^{92}\text{Zr}(\gamma, 3\text{n})/^{27}\text{Al}(\gamma, n)$<br><i>i.e.</i> $(27.8-E_\gamma)/(31.4-E_\gamma)$          | –     | –     | –     | 1.399 | 1.312 | 1.265 | 1.226 | 1.182 |
| $^{90}\text{Zr}(\gamma, 2\text{n})/^{27}\text{Al}(\gamma, 2\text{pn})$<br><i>i.e.</i> $(21.3-E_\gamma)/(31.4-E_\gamma)$ | –     | –     | –     | 2.372 | 2.059 | 1.893 | 1.772 | 1.618 |
| $^{91}\text{Zr}(\gamma, 3\text{n})/^{27}\text{Al}(\gamma, 2\text{pn})$<br><i>i.e.</i> $(28.5-E_\gamma)/(31.4-E_\gamma)$ | –     | –     | –     | 1.324 | 1.260 | 1.218 | 1.185 | 1.150 |
| $^{92}\text{Zr}(\gamma, 4\text{n})/^{27}\text{Al}(\gamma, 2\text{pn})$<br><i>i.e.</i> $(37.1-E_\gamma)/(31.4-E_\gamma)$ | –     | –     | –     | 0.467 | 0.594 | 0.670 | 0.713 | 0.762 |
| $^{90}\text{Zr}(\gamma, 3\text{n})/^{27}\text{Al}(\gamma, 2\text{pn})$<br><i>i.e.</i> $(33.6-E_\gamma)/(31.4-E_\gamma)$ | –     | –     | –     | 0.764 | 0.829 | 0.863 | 0.879 | 0.898 |
| $^{91}\text{Zr}(\gamma, 4\text{n})/^{27}\text{Al}(\gamma, n)$<br><i>i.e.</i> $(40.8-E_\gamma)/(31.4-E_\gamma)$          | –     | –     | –     | –     | –     | 0.478 | 0.548 | 0.627 |
| $^{90}\text{Zr}(\gamma, 4\text{n})/^{27}\text{Al}(\gamma, 2\text{pn})$<br><i>i.e.</i> $(43.2-E_\gamma)/(31.4-E_\gamma)$ | –     | –     | –     | 0.063 | 0.244 | 0.365 | 0.456 | 0.552 |
| $^{91}\text{Zr}(\gamma, 5\text{n})/^{27}\text{Al}(\gamma, n)$<br><i>i.e.</i> $(50.5-E_\gamma)/(31.4-E_\gamma)$          | –     | –     | –     | –     | 0.100 | 0.211 | 0.296 | 0.356 |

All the terms in eq. (3) have the similar meaning as in eq. (1). As can be seen from table 1, in the case of the  $^{\text{nat}}\text{Zr}(\gamma, \text{xn})^{89}\text{Zr}$  reaction, both meta-stable (m) and ground (g) state have suitable half-lives with high-intensity  $\gamma$ -rays. Thus, the  $^{\text{nat}}\text{Zr}(\gamma, \text{xn})^{89}\text{Zr}$  reaction cross-sections for both m- and g-states and thus the total cross-section were obtained at the bremsstrahlung end-point energies of 16 and 45–70 MeV. The reaction product  $^{88}\text{Zr}$  has a half-life of 83.4 d with  $\gamma$ -rays of very low intensity. In spite of that, the  $^{\text{nat}}\text{Zr}(\gamma, \text{xn})^{88}\text{Zr}$  reaction cross-section was possible to measure in the present work at the bremsstrahlung end-point energies of 45–70 MeV. The reaction products  $^{87}\text{Zr}$  and  $^{86}\text{Zr}$  have the half-lives of 1.68 h and 16.5 h with very good intensities of the  $\gamma$ -rays. Thus, the  $^{\text{nat}}\text{Zr}(\gamma, \text{xn})^{87}\text{Zr}$  and  $^{\text{nat}}\text{Zr}(\gamma, \text{xn})^{86}\text{Zr}$  reaction cross-sections were measured at the bremsstrahlung end-point energies of 45–70 MeV. In the case of the  $^{\text{nat}}\text{Zr}(\gamma, n)^{95}\text{Zr}$

reaction,  $^{95}\text{Zr}$  has the half-life of 64.02 d with very good intensities of the  $\gamma$ -rays. Besides this,  $^{95}\text{Zr}$  is produced only from the  $^{96}\text{Zr}(\gamma, n)^{95}\text{Zr}$  reaction. There is no contributions from the other isotopes and thus the  $^{96}\text{Zr}(\gamma, n)^{95}\text{Zr}$  reaction cross-section was updated to 100%  $^{96}\text{Zr}$ . In the cases of  $^{\text{nat}}\text{Zr}(\gamma, \text{xn})^{88-86}\text{Zr}$  reactions, there are some contributions from other isotopes but more than 93% is from 51.45%  $^{90}\text{Zr}$  except  $^{90}\text{Zr}(\gamma, 3\text{n})^{87}\text{Zr}$ , where it is 88%. The percentage of contribution for different reactions channels, *i.e.* the yield ( $Y_i$ ) can be calculated using the relation [47]

$$Y_i = \int_{E_{\text{th}}}^{E_{\text{max}}} C_i \sigma_i(E) \varphi(E) dE / \sum \int_{E_{\text{th}}}^{E_{\text{max}}} C_i \sigma_i(E) \varphi(E) dE, \quad (5)$$

where  $C_i$  is the natural composition of the isotope in the  $i$ -th nuclear reaction,  $\sigma_i$  is the reaction cross-section and  $\varphi(E)$  is the photon flux at energy  $E$ .

**Table 3.** The percentage of formation cross-section (yields) of the different reaction products from the  $^{\text{nat}}\text{Zr}(\gamma, \text{xn})$  reactions calculated using TALYS [31].

| Reactions   | 12  | 14  | 16  | 45     | 50     | 55     | 60     | 70     |
|---|-----|-----|-----|--------|--------|--------|--------|--------|
| $^{96}\text{Zr}(\gamma, \text{n})^{95}\text{Zr}$  | 100 | 100 | 100 | 100    | 100    | 100    | 100    | 100    |
| $^{90}\text{Zr}(\gamma, \text{n})^{89}\text{Zr}$  | 100 | 100 | 100 | 97.254 | 97.092 | 96.905 | 96.723 | 96.455 |
| $^{91}\text{Zr}(\gamma, 2\text{n})^{89}\text{Zr}$ | –   | –   | –   | 2.216  | 2.200  | 2.281  | 2.344  | 2.415  |
| $^{92}\text{Zr}(\gamma, 3\text{n})^{89}\text{Zr}$ | –   | –   | –   | 0.580  | 0.703  | 0.782  | 0.850  | 0.950  |
| $^{94}\text{Zr}(\gamma, 5\text{n})^{89}\text{Zr}$ | –   | –   | –   | –      | 0.005  | 0.033  | 0.083  | 0.180  |
| $^{90}\text{Zr}(\gamma, 2\text{n})^{88}\text{Zr}$ | –   | –   | –   | 96.158 | 95.061 | 94.281 | 93.566 | 92.556 |
| $^{91}\text{Zr}(\gamma, 3\text{n})^{88}\text{Zr}$ | –   | –   | –   | 3.810  | 4.696  | 5.094  | 5.385  | 5.693  |
| $^{92}\text{Zr}(\gamma, 4\text{n})^{88}\text{Zr}$ | –   | –   | –   | 0.032  | 0.430  | 0.625  | 1.044  | 1.617  |
| $^{94}\text{Zr}(\gamma, 6\text{n})^{88}\text{Zr}$ | –   | –   | –   | –      | 0.001  | 0.005  | 0.036  | 0.140  |
| $^{90}\text{Zr}(\gamma, 3\text{n})^{87}\text{Zr}$ | –   | –   | –   | 99.761 | 97.859 | 95.347 | 92.597 | 87.987 |
| $^{91}\text{Zr}(\gamma, 4\text{n})^{87}\text{Zr}$ | –   | –   | –   | 0.239  | 2.141  | 4.588  | 6.696  | 8.563  |
| $^{92}\text{Zr}(\gamma, 5\text{n})^{88}\text{Zr}$ | –   | –   | –   | –      | –      | 0.066  | 0.706  | 3.435  |
| $^{94}\text{Zr}(\gamma, 7\text{n})^{87}\text{Zr}$ | –   | –   | –   | –      | –      | –      | –      | 0.015  |
| $^{90}\text{Zr}(\gamma, 4\text{n})^{86}\text{Zr}$ | –   | –   | –   | 100    | 100    | 99.921 | 98.850 | 94.407 |
| $^{91}\text{Zr}(\gamma, 5\text{n})^{86}\text{Zr}$ | –   | –   | –   | –      | –      | 0.079  | 1.150  | 5.304  |
| $^{92}\text{Zr}(\gamma, 6\text{n})^{86}\text{Zr}$ | –   | –   | –   | –      | –      | –      | 0.016  | 0.289  |

The theoretical reaction cross-section ( $\sigma_i$ ) for different reaction channels from  $^{\text{nat}}\text{Zr}$  was calculated using TALYS 1.4 [31] code, which is described in the next section. Then the normalized yield contribution to a particular product from reactions of different isotopes is shown in table 3. It can be seen, from table 3, that more than 88–93% formation cross-sections of  $^{89}\text{Zr}$ ,  $^{88}\text{Zr}$ ,  $^{87}\text{Zr}$  and  $^{86}\text{Zr}$  comes from the  $(\gamma, \text{n})$ ,  $(\gamma, 2\text{n})$ ,  $(\gamma, 3\text{n})$  and  $(\gamma, 4\text{n})$  reaction of the 51.45% of  $^{90}\text{Zr}$  in the  $^{\text{nat}}\text{Zr}$ .

## 4 Results and discussion

The  $^{\text{nat}}\text{Zr}(\gamma, \text{xn})^{89-86}\text{Zr}$  and  $^{96}\text{Zr}(\gamma, \text{n})^{95}\text{Zr}$  reaction cross-sections determined in the present work at the bremsstrahlung end-point energies of 12, 14, 16, 45, 50, 55, 60 and 70 MeV are given in table 4 along with the literature data at 10, 12.5 and 32 MeV [29,30]. In table 4, the  $^{\text{nat}}\text{Zr}(\gamma, \text{n})^{89}\text{Zr}$  and  $^{96}\text{Zr}(\gamma, \text{n})^{95}\text{Zr}$  reaction cross-sections at the bremsstrahlung end-point energies of 10–16 and 45–70 MeV are based on the weighted average flux of the  $^{197}\text{Au}(\gamma, \text{n})^{196}\text{Au}$  reaction cross-section of mono-energetic photon from ref. [45] and from TALYS [31]. On the other hand, the  $^{\text{nat}}\text{Zr}(\gamma, \text{xn})^{88}\text{Zr}$ ,  $^{\text{nat}}\text{Zr}(\gamma, \text{xn})^{87}\text{Zr}$  and  $^{\text{nat}}\text{Zr}(\gamma, \text{xn})^{86}\text{Zr}$  reaction cross-sections at the bremsstrahlung end-point energies of 45–70 MeV are based on the weighted average flux of the  $^{27}\text{Al}(\gamma, 2\text{pn})^{24}\text{Na}$  reaction cross-section [46]. The uncertainties associated to the measured cross-sections come from the replicate measurements. The overall uncertainty is the quadratic sum of both random and systematic errors. The random error in the observed activity is primarily due to counting statistics, which is estimated to be 5–10%. This can be determined by accumulating the data for an optimum time period that

depends on the half-life of the nuclides of interest. The systematic errors are due to uncertainties in photon flux estimate ( $\sim 2\%$ ), the irradiation time ( $\sim 0.5\%$ ), the detection efficiency calibration ( $\sim 3\%$ ), the half-life of the reaction products and the  $\gamma$ -ray abundances ( $\sim 2\%$ ). Thus the total systematic error is about  $\sim 4.15\%$ . The overall uncertainty is found to be between 6.5 and 10.8%, coming from the combination of a statistical error of 5–10% and a systematic error of 4.15%.

The  $^{\text{nat}}\text{Zr}(\gamma, \text{xn})^{89-86}\text{Zr}$  reaction cross-sections at the bremsstrahlung end-point energies of 16, 45, 50, 55, 60 and 70 MeV from the present work were determined for the first time. Similarly, the  $^{96}\text{Zr}(\gamma, \text{n})^{95}\text{Zr}$  reaction cross-section at bremsstrahlung end-point energies of 12–16 and 45–70 MeV are also determined for the first time. In the literature, there are only three values at the bremsstrahlung end-point energies of 10, 12.5 and 32 MeV [29,30] based on the activation and off-line  $\gamma$ -ray spectrometric technique. Besides this, the  $^{90}\text{Zr}(\gamma, \text{xn})^{89,88}\text{Zr}$  and  $^{96}\text{Zr}(\gamma, \text{n})^{95}\text{Zr}$  reaction cross-sections for the mono-energetic photons within 26 MeV are available in the literature [20–28]. For the  $^{\text{nat}}\text{Zr}(\gamma, \text{xn})^{87,86}\text{Zr}$  reaction cross-sections, there are no data available in the literature even based on the mono-energetic photons. Thus the  $^{\text{nat}}\text{Zr}(\gamma, \text{xn})^{95,89-86}\text{Zr}$  reaction cross-sections as a function of photon energy were calculated using TALYS code 1.4 [31].

TALYS is a computer code basically used to calculate the nuclear reaction cross-sections that involve the projectiles like neutrons, photons, protons, deuterons, tritons,  $^3\text{He}$ - and alpha-particles, in the energy range of 1 keV to 200 MeV and for target nuclides of mass 12 and heavier.

**Table 4.**  $^{96}\text{Zr}(\gamma, n)^{95}\text{Zr}$ ,  $^{\text{nat}}\text{Zr}(\gamma, xn)^{89\text{m.g}}\text{Zr}$ ,  $^{\text{nat}}\text{Zr}(\gamma, xn)^{88}\text{Zr}$ ,  $^{\text{nat}}\text{Zr}(\gamma, xn)^{87}\text{Zr}$  and  $^{\text{nat}}\text{Zr}(\gamma, xn)^{86}\text{Zr}$  reactions cross-sections at the bremsstrahlung end-point energies of 10–16 and 45–70 MeV from present work and flux-weighted values from literature data [20–30] and TALYS [31].

| Reactions  | Bremsstrahlung energy (MeV) | Ref.      | Average reaction cross-section from threshold ( $E_{\text{th}}$ ) to end-point ( $E_e$ ) bremsstrahlung energy ( $\langle\sigma\rangle = \sum_{E_{\text{th}}}^{E_e} Y_{i\sigma i}$ ) in mb |                  |                     |            |
|--|-----------------------------|-----------|--|------------------|---------------------|------------|
|  |                             |           | Experimental   |                  |                     | TALYS [28] |
|  |                             |           | Meta-stable state  | Ground state     | Total               | Total      |
| $^{96}\text{Zr}(\gamma, n)^{95}\text{Zr}$          | 10                          | [30]      | –  | –                | $16.94 \pm 0.98$    | 13.17      |
|  | 12                          | This work | –  | –                | $24.18 \pm 1.41$    | 18.00      |
|  | 12.5                        | [30]      | –  | –                | $32.99 \pm 0.45$    | 19.96      |
|  | 14                          | This work | –  | –                | $34.66 \pm 2.79$    | 27.66      |
|  | 16                          | This work | –  | –                | $42.00 \pm 2.73$    | 39.36      |
|  | 45                          | This work | –  | –                | $28.25 \pm 1.85$    | 27.22      |
|  | 50                          | This work | –  | –                | $27.58 \pm 1.71$    | 26.01      |
|  | 55                          | This work | –  | –                | $25.72 \pm 1.98$    | 24.60      |
|  | 60                          | This work | –  | –                | $24.34 \pm 1.35$    | 23.54      |
|  | 70                          | This work | –  | –                | $22.87 \pm 2.33$    | 22.70      |
| $^{\text{nat}}\text{Zr}(\gamma, xn)^{89}\text{Zr}$ | 16                          | This work | $13.30 \pm 0.59$   | $11.40 \pm 0.08$ | $24.70 \pm 0.79$    | 28.44      |
|  | 32                          | [29]      | –  | –                | $34.88 \pm 1.60$    | 33.72      |
|  | 32                          | [22]      | –  | –                | $38.33 \pm 1.44$    | 33.72      |
|  | 32                          | [20]      | –  | –                | $30.66 \pm 1.44$    | 33.72      |
|  | 45                          | This work | $14.53 \pm 0.44$   | $12.14 \pm 0.80$ | $25.77 \pm 0.91$    | 26.87      |
|  | 50                          | This work | $13.07 \pm 0.58$   | $11.80 \pm 0.70$ | $24.42 \pm 0.91$    | 24.46      |
|  | 55                          | This work | $12.96 \pm 0.47$   | $11.98 \pm 0.71$ | $24.14 \pm 0.85$    | 23.12      |
|  | 60                          | This work | $11.75 \pm 0.52$   | $11.90 \pm 0.85$ | $22.91 \pm 0.95$    | 21.87      |
|  | 70                          | This work | $10.26 \pm 0.51$   | $11.50 \pm 0.54$ | $21.12 \pm 0.74$    | 20.01      |
| $^{\text{nat}}\text{Zr}(\gamma, xn)^{88}\text{Zr}$ | 45                          | This work | –  | –                | $3.73 \pm 0.26$     | 3.86       |
|  | 50                          | This work | –  | –                | $3.22 \pm 0.26$     | 3.56       |
|  | 55                          | This work | –  | –                | $3.33 \pm 0.33$     | 3.36       |
|  | 60                          | This work | –  | –                | $3.19 \pm 0.28$     | 3.16       |
|  | 70                          | This work | –  | –                | $2.80 \pm 0.31$     | 2.91       |
| $^{\text{nat}}\text{Zr}(\gamma, xn)^{87}\text{Zr}$ | 45                          | This work | –  | –                | $0.71 \pm 0.14$     | 0.64       |
|  | 50                          | This work | –  | –                | $0.84 \pm 0.18$     | 0.78       |
|  | 55                          | This work | –  | –                | $0.88 \pm 0.15$     | 0.82       |
|  | 60                          | This work | –  | –                | $1.07 \pm 0.22$     | 0.81       |
|  | 70                          | This work | –  | –                | $0.89 \pm 0.17$     | 0.78       |
| $^{\text{nat}}\text{Zr}(\gamma, xn)^{86}\text{Zr}$ | 45                          | This work | –  | –                | $0.0027 \pm 0.0002$ | 0.0022     |
|  | 50                          | This work | –  | –                | $0.061 \pm 0.004$   | 0.064      |
|  | 55                          | This work | –  | –                | $0.158 \pm 0.017$   | 0.163      |
|  | 60                          | This work | –  | –                | $0.194 \pm 0.019$   | 0.230      |
|  | 70                          | This work | –  | –                | $0.279 \pm 0.029$   | 0.279      |

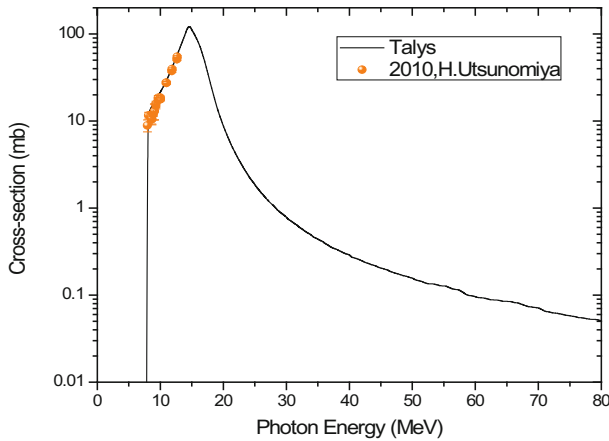


**Fig. 5.** Cross-sections of the  $^{96}\text{Zr}(\gamma, n)^{95}\text{Zr}$  reaction as a function of gamma energy obtained from the experimental data [27] and the calculated values from the TALYS [31] based on the mono-energetic photons, which are shown with continuous lines.

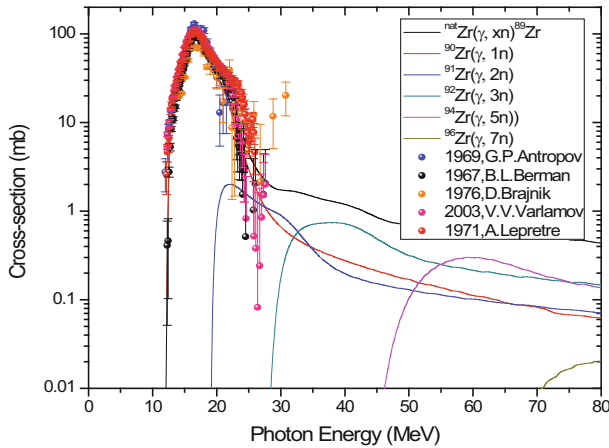


**Fig. 6.** Cross-sections of the  $^{\text{nat}}\text{Zr}(\gamma, xn)^{89}\text{Zr}$  reaction as a function of gamma energy obtained from the experimental data [20–26] and the calculated values from the TALYS [31] based on the mono-energetic photons, which are shown with continuous lines.

In TALYS, the reactions cross-section to all open channels can be calculated. Several options are included for the choice of different parameters such as  $\gamma$ -ray strength functions, nuclear level densities and nuclear model parameters, etc. In the present work, we calculated the  $^{\text{nat}}\text{Zr}(\gamma, xn)$  reaction cross-section using the default option in the TALYS code [31]. All possible outgoing channels for the given photon energy were considered. However, the cross-sections for the  $(\gamma, n)$ ,  $(\gamma, 2n)$ ,  $(\gamma, 3n)$  and  $(\gamma, 4n)$  reactions from different isotopes of Zr were collected. Then the formation cross-section of  $^{95}\text{Zr}$ ,  $^{89}\text{Zr}$ ,  $^{88}\text{Zr}$ ,  $^{87}\text{Zr}$  and  $^{86}\text{Zr}$  from different reaction channels of the Zr isotopes and the total formation cross-sections of each reaction products are plotted in figs. 5–9 as a function of photon energy. The experimental  $^{96}\text{Zr}(\gamma, n)^{95}\text{Zr}$ ,  $^{90}\text{Zr}(\gamma, n)^{89}\text{Zr}$  and  $^{90}\text{Zr}(\gamma, 2n)^{88}\text{Zr}$  reaction cross-sections from refs. [20–30] are also plotted in figs. 5–9 for compar-

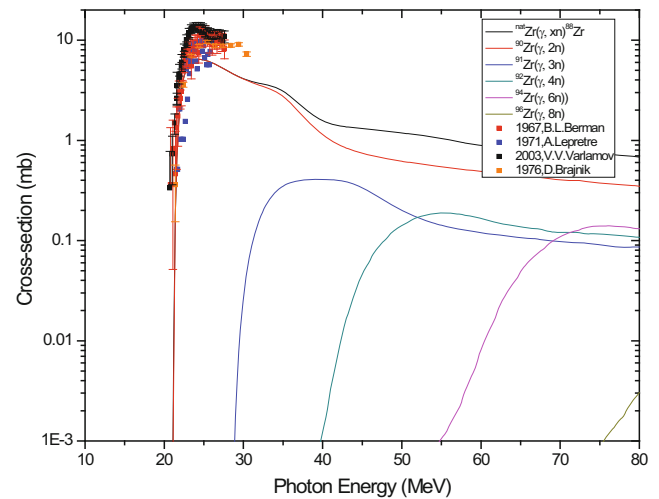


**Fig. 7.** Cross-sections of the  $^{\text{nat}}\text{Zr}(\gamma, xn)^{88}\text{Zr}$  reaction as a function of gamma energy obtained from the experimental data [20–26] and the calculated values from the TALYS [31] based on the mono-energetic photons, which are shown with continuous lines.

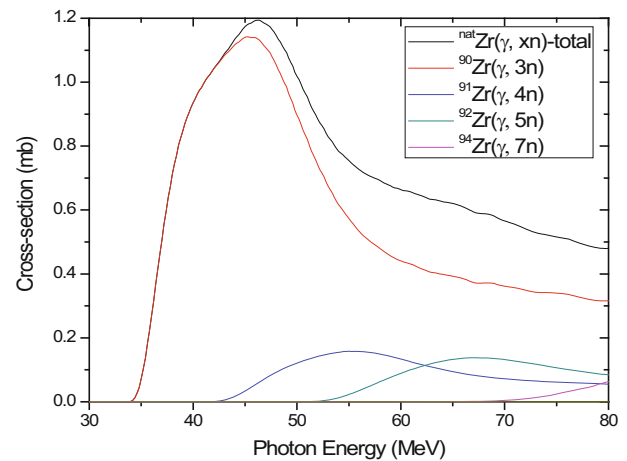


**Fig. 8.** Cross-sections of the  $^{\text{nat}}\text{Zr}(\gamma, xn)^{87}\text{Zr}$  reaction as a function of gamma energy obtained from the calculated values of the TALYS [31] based on mono-energetic photons, which are shown with continuous lines.

ison. It can be seen, from figs. 5–7, that the theoretical  $^{96}\text{Zr}(\gamma, n)^{95}\text{Zr}$ ,  $^{90}\text{Zr}(\gamma, n)^{89}\text{Zr}$  and  $^{90}\text{Zr}(\gamma, 2n)^{88}\text{Zr}$  reaction cross-sections as a function of photon energy from TALYS 1.4 show a similar structure of the available experimental data [20–28]. However, in the literature no experimental data for the  $^{90}\text{Zr}(\gamma, 3n)^{87}\text{Zr}$  and  $^{90}\text{Zr}(\gamma, 4n)^{86}\text{Zr}$  reactions are available to compare with the theoretical data of TALYS.

In order to compare with the present data, the flux-weighted average  $^{96}\text{Zr}(\gamma, n)^{95}\text{Zr}$   $^{\text{nat}}\text{Zr}(\gamma, xn)^{89-86}\text{Zr}$  reaction cross-sections were obtained from the literature data [20–28] and theoretical values of TALYS 1.4 based on mono-energetic photon by using eq. (2). Those values at different bremsstrahlung end-point energies are given in table 4 and plotted in fig. 10. It can be

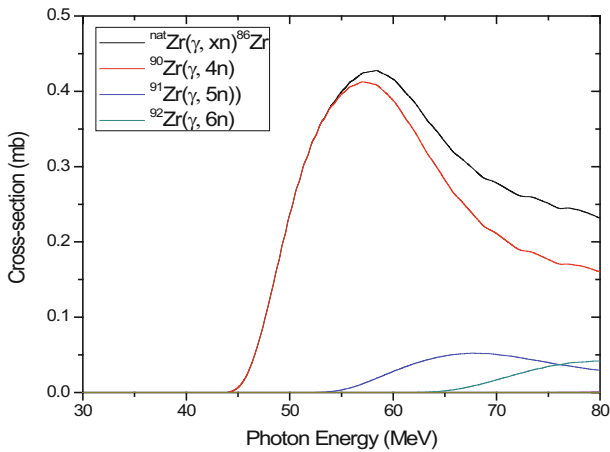


**Fig. 9.** Cross-sections of the  ${}^{\text{nat}}\text{Zr}(\gamma, \text{xn}){}^{86}\text{Zr}$  reaction as a function of gamma energy obtained from the calculated values of the TALYS [31] based on mono-energetic photons, which are shown with continuous lines.

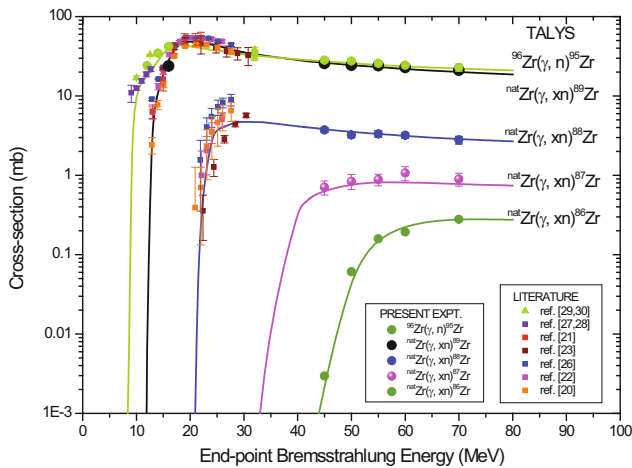


**Fig. 10.** Cross-sections of the  ${}^{\text{nat}}\text{Zr}(\gamma, \text{xn})$  reactions of the present work as a function of end-point bremsstrahlung energies and the flux-weighted literature data [20–30] and the calculated values of the TALYS [31] based on mono-energetic photons, which are shown with continuous lines.

seen from table 4 that the experimentally obtained flux-weighted average  ${}^{96}\text{Zr}(\gamma, \text{n}){}^{95}\text{Zr}$ ,  ${}^{90}\text{Zr}(\gamma, \text{n}){}^{89}\text{Zr}$  and  ${}^{90}\text{Zr}(\gamma, 2\text{n}){}^{88}\text{Zr}$  reaction cross-sections of the present work at the bremsstrahlung end-point energies of 10–16 MeV are in good agreement with the flux-weighted value of TALYS [31] and literature data [20–28]. However, there is no data available in the literature to compare with the experimental data of  ${}^{96}\text{Zr}(\gamma, \text{n}){}^{95}\text{Zr}$  and  ${}^{\text{nat}}\text{Zr}(\gamma, \text{xn}){}^{89-86}\text{Zr}$  reactions cross-sections at the bremsstrahlung end-point energies of 45–70 MeV. On the other hand, it can be seen, from fig. 10, that the experimentally obtained  ${}^{96}\text{Zr}(\gamma, \text{n}){}^{95}\text{Zr}$  and  ${}^{\text{nat}}\text{Zr}(\gamma, \text{xn}){}^{89-86}\text{Zr}$  reaction cross-sections at the bremsstrahlung end-point energies of 12–16 and 45–70 MeV from the present work and literature data [29,30] at 10, 12.5 and 32 MeV are in good agreement with the flux-weighted TALYS values within the uncertainty limits.

Further, it can be seen from fig. 10 that the experimental and theoretical  ${}^{96}\text{Zr}(\gamma, \text{n}){}^{95}\text{Zr}$  and  ${}^{\text{nat}}\text{Zr}(\gamma, \text{xn}){}^{89}\text{Zr}$  reaction cross-sections increase very sharply from the threshold values to 16–22 MeV, *i.e.* where the  $(\gamma, 2\text{n})$  channel opens up. Above 16–22 MeV, it increases slowly and remains constant up to 24–34 MeV, *i.e.* where the  ${}^{\text{nat}}\text{Zr}(\gamma, \text{xn}){}^{88}\text{Zr}$  reaction channels opens up. There after the cross-section slowly decreases up to bremsstrahlung end-point energy of 70 MeV. This is due to the opening of other reactions channels. Similarly, the experimental and theoretical  ${}^{\text{nat}}\text{Zr}(\gamma, \text{xn}){}^{88}\text{Zr}$  reaction cross-section increases very sharply from the threshold value of 22 MeV to 28 MeV. Above 28 MeV, it increases very slowly up to 32 MeV and then remains constant up to 44 MeV, *i.e.* up to the opening of  ${}^{\text{nat}}\text{Zr}(\gamma, \text{xn}){}^{87,86}\text{Zr}$  reaction channel. There after the cross-section slowly decreases up to the bremsstrahlung end-point energy of 70 MeV. This is due to the opening of other reactions channels. The theoretical and experimental  ${}^{\text{nat}}\text{Zr}(\gamma, \text{xn}){}^{87,86}\text{Zr}$  reaction cross-sections also shows similar trend (fig. 10) as of  ${}^{96}\text{Zr}(\gamma, \text{n}){}^{95}\text{Zr}$  and  ${}^{\text{nat}}\text{Zr}(\gamma, \text{xn}){}^{89,88}\text{Zr}$  reaction channels. First, it increases sharply from its respective threshold value to a particular value and remains constant to a certain extent, where other reaction channels start increasing. Then it starts decreasing due to the contribution of excitation energy to the other reaction channels. The above observations indicate the role of excitation energy and its partition in to different reaction channels. Besides the above observations, it can be seen from fig. 10 that the increasing trend of cross-section from threshold value up to the excitation energy of the next channel are more pronounced for the  ${}^{96}\text{Zr}(\gamma, \text{n}){}^{95}\text{Zr}$  and  ${}^{\text{nat}}\text{Zr}(\gamma, \text{xn}){}^{89,88}\text{Zr}$  reactions compared to the  ${}^{\text{nat}}\text{Zr}(\gamma, \text{xn}){}^{87,86}\text{Zr}$  reactions. This is because the increasing trend of the  ${}^{96}\text{Zr}(\gamma, \text{n}){}^{95}\text{Zr}$  and  ${}^{\text{nat}}\text{Zr}(\gamma, \text{xn}){}^{89,88}\text{Zr}$  reaction cross-sections lies within 10–25 MeV, where GDR effect plays its role besides excitation energy.

## 5 Conclusions

i) The  ${}^{96}\text{Zr}(\gamma, \text{n}){}^{95}\text{Zr}$  and  ${}^{\text{nat}}\text{Zr}(\gamma, \text{xn}){}^{89}\text{Zr}$  reaction cross-sections at the bremsstrahlung end-point energies of 12–16 MeV has been determined using activation and off-line  $\gamma$ -ray spectrometric technique. Similarly, the  ${}^{96}\text{Zr}(\gamma, \text{n}){}^{95}\text{Zr}$  and  ${}^{\text{nat}}\text{Zr}(\gamma, \text{xn}){}^{89-86}\text{Zr}$  reactions cross-sections at the end-point bremsstrahlung energies of 45–70 MeV were also determined using the same technique.

ii) The  ${}^{96}\text{Zr}(\gamma, \text{n}){}^{95}\text{Zr}$  and  ${}^{\text{nat}}\text{Zr}(\gamma, \text{xn}){}^{89-86}\text{Zr}$  reaction cross-sections as a function of mono-energetic photon energy was theoretically calculated using the TALYS 1.4 code. The flux-weighted average reaction cross-sections at different bremsstrahlung end-point energies were then obtained from the theoretical values of TALYS and the literature data based on mono-energetic photon and are found to be in good agreement.

iii) The experimental and theoretical  ${}^{96}\text{Zr}(\gamma, \text{n}){}^{95}\text{Zr}$  and  ${}^{\text{nat}}\text{Zr}(\gamma, \text{xn}){}^{89-86}\text{Zr}$  reaction cross-sections increase from the threshold value to a certain value, where another reaction channel opens up. Then it remains constant up

to certain energy, where other reaction starts increasing. There after they decrease, when the higher reaction channels remain constant. This indicates the effect of excitation energy and its partition in different reaction channels.

iv) Within the end-point bremsstrahlung of 25 MeV, the increasing trend of cross-sections for the  $^{96}\text{Zr}(\gamma, n)^{95}\text{Zr}$  and  $^{\text{nat}}\text{Zr}(\gamma, xn)^{89,88}\text{Zr}$  reactions is sharper than for the  $^{\text{nat}}\text{Zr}(\gamma, xn)^{87,86}\text{Zr}$  reactions. This indicates pronounced GDR effect besides the role of excitation energy within the bremsstrahlung end-point energy of 25 MeV.

The authors are thankful to the staff of the electron linacs ELBE at HZDR, Dresden, Germany and PAL, Pohang, Korea for providing the electron beam to carry out the experiments. One of the authors, HN, is thankful to the Brain pool program under KOFEST, Korea for inviting him as a visiting professor to the department of high energy physics, Daegu as well as for giving financial support to travel to Dresden, Germany to carry out the experiment. This research was partly supported by the National Research Foundation of Korea (NRF) through a grant provided by the Korean Ministry of Science, ICT and Future Planning (NRF-2013R1A2A2A01067340), by the Institutional Activity Program of Korea Atomic Energy Research Institute, and by the National R&D Program through the Dong-nam Institute of Radiological & Medical Sciences (50491-2014).

## References

1. F. Carminati, R. Klapisch, J.P. Revol, J.A. Rubia, C. Rubia, CERN/AT/93-49 (ET) 1993.
2. C. Rubia, J.A. Rubio, S. Buono, F. Carminati, N. Fietier, J. Galvez, C. Geles, Y. Kadi, R. Klapisch, P. Mandrillon, J.P. Revol, Ch. Roche, CERN/AT/95-44 (ET) 1995, CERN/AT/95-53 (ET) 1995, CERN/LHC/96-01 (LET) 1996, CERN/LHC/97-01 (EET) 1997.
3. C.D. Bowman, in *Proceedings of the International Conference on Accelerator-Drive Transmutation Technologies and Applications, Las Vegas, NV, USA, 1994*, AIP Conf. Proc., Vol. **346** (AIP, 1995).
4. Accelerator Driven Systems: Energy Generation and Transmutation of Nuclear Waste, Status report, IAEA, Vienna, IAEA-TECDO-985 (1997).
5. C.D. Bowman, *Annu. Rev. Nucl. Part Sci.* **48**, 505 (1998).
6. S. Ganesan, Pramana, *J. Phys.* **68**, 257 (2007).
7. J. Adam, A.R. Balabekyan, V.S. Barashenkov, R. Brandt, V.M. Golovatiouk, V.G. Kalinnikov, K. Katovsky, M.I. Krivopustov, V. Kumar, H. Kumawat, R. Odoj, V.S. Pronskikh, A.A. Solnyshkin, V.I. Stegailov, V.M. Tsoupko-Sitnikov, W. Westmeier, *Eur. Phys. J. A* **23**, 61 (2005).
8. *DOE Fundamentals handbook material science*, Vol. **2** of 2 DOE-HDBK-1017/2-93 January, U.S. Department of Energy FSC-6910 Washington, D.C. 20585 (1993).
9. R.H. Zee, M.W. Guinan, J.S. Huang, *J. Nucl. Mater.* **141-143**, 874 (1986).
10. N. Stojilovic, E.T. Bender, R.D. Ramsier, *Progr. Surf. Sci.* **78**, 101 (2005).
11. *IAEA Delayed hydride cracking in zirconium alloys in pressure tube nuclear reactors*, Final report of a coordinated research project: IAEA TECDOC-1410, available online at <http://www-nds.iaea.org>.
12. G.R. Pansare, P.M. Digheand, V.N. Bhoraskar, *Radiat. Phys. Chem.* **40**, 213 (1992).
13. F.M.D. Attar, R. Mandal, S.D. Dhole, A. Saxena, Ashokkumar, S. Ganesan, S. Kailas, V.N. Bhoraskar, *Nucl. Phys. A* **802**, 1 (2008).
14. E.T. Anderson, S.A. Wilson, J.H. Schemel, United States Patent 4, 908, 071 (1990).
15. P. Patnaik, *Handbook of Inorganic Chemicals* (The McGraw-Hill, 2003) pp. 995.
16. L.L. Shreir, R.A. Jarman, G.T. Burstein, *Corrosion*, third edition, Vol. **1** (Butterworth-Heinemann, Oxford, 1994).
17. P. Rudling, A. Strasser, F. Garzarolli, *IZNA7 Special topic report welding of zirconium alloys* (2007).
18. *IAEA Handbook on photonuclear data for applications cross-sections and spectra*, IAEA-TECDOC-1178, available online at <http://www-nds.iaea.org>.
19. *IAEA-EXFOR, Experimental Nuclear Reaction Data*, available online at <http://www-nds.iaea.org/exfor>.
20. B.L. Berman, J.T. Caldwell, R.R. Harvey, M.A. Kelly, R.L. Bramblett, S.C. Fultz, *Phys. Rev.* **162**, 1098 (1967).
21. G.P. Antropov, I.E. Mitrofanov, A.I. Prokof'ev, B.S. Russkikh, *Izv. Rossiiskoi Akad. Nauk, Ser. Fiz.* **33**, 700 (1969).
22. A. Lepretre, H. Beil, R. Bergere, P. Carlos, A. Veyssiere, *Nucl. Phys. A* **75**, 609 (1971).
23. D. Brajnik, D. Jamnik, G. Kernel, M. Korun, U. Miklavzic, B. Pucelj, A. Stanovnik, *Phys. Rev. C* **13**, 1852 (1976).
24. A. Veyssiere, H. Beil, R. Bergere, P. Carols, J. Fagot, A. Lepretreand A. de Miniac, *Z. Phys. A At. Nucl.* **306**, 139 (1982).
25. B.L. Berman, R.E. Pywell, S.S. Dietrich, M.N. Thompson, K.G. Mc Neill, J.W. Jury, *Phys. Rev. C* **36**, 1286 (1987).
26. V.V. Varlamov, N.N. Peskov, D.S. Rudenko, M.E. Stepanov, *Vop. At. Naukii Tekhn. Ser. Yadernye Konstanty* **2003**, 48 (2003).
27. H. Utsunomiya, S. Goriely, T. Kondo, T. Kaihoti, A. Maki-naga, S. Goko, H. Akimune, T. Yamagata, H. Toyokawa, T. Mstsumoto, H. Harano, S. Hohara, Y.-W. Lui, S. Hilaire, S. Peruand, A.J. Koning, *Phys. Rev. Lett.* **100**, 162502 (2008).
28. H. Utsunomiya, S. Goriely, H. Akimune, H. Harada, F. Kitatani, S. Goko, H. Toyokawa, K. Yamada, T. Kondo, O. Itoh, M. Kamata, T. Yamagata, Y.-W. Lui, S. Hilaireand, A.J. Koning, *Phys. Rev. C* **81**, 035801 (2010).
29. A.K. Md. L. Rahman, K. Kato, H. Arima, N. Shigyo, K. Ishibashi, J. Hori, K. Nakajima, *J. Nucl. Sci. Tech.* **47**, 618 (2010).
30. R. Crasta, H. Naik, S.V. Suryanarayana, Ganesh Sanjeev, P.M. Prajapati, M. Kumar, T.N. Nathaniel, V.T. Nimje, K.C. Mittaland, A. Goswami, *Radiochim. Acta* **102**, 221 (2014) DOI:10.1515/ract-2014-2122.
31. A.J. Koning, S. Hilaire, M.C. Duijvestijn, in *Proceedings of the International Conference on Nuclear Data for Science and Technology, ND 2004*, edited by R.C. Haight, M.B. Chadwick, T. Kawano, P. Talou, AIP Vol. **769** (2004), p. 1154.
32. M. Erhard, A.R. Junghans, C. Nair, R. Schwengner, R. Beyer, J. Klug, K. Kosev, A. Wagner, *Phys. Rev. C* **81**, 034319 (2010).
33. R. Schwengner, R. Beyer, F. Donau, E. Gosse, A. Hartmann, A.R. Junghans, S. Mallian, G. Rusev, K.D. Schilling, W. Schulze, A. Wagner, *Nuc. Instrum. Methods Phys. A* **555**, 211 (2005).

34. H. Naik, Sarbjit Singh, A. Goswami, V.K. Manchanda, G. Kim, K.S. Kim, M.W. Lee, Md. ShakilurRahman, D. Raj, S. Ganesan, S.V. Suryanarayana, M.H. Cho, W. Namkung, Nucl. Instrum. Methods Phys. Res. B **269**, 1417 (2011).
35. C.F. Weizsäcker, Z. Phys. **88**, 612 (1934).
36. E.J. Williams, Phys. Rev. **45**, 729 (1934).
37. E. Browne, R.B. Firestone, in *Table of Radioactive Isotopes*, edited by V.S. Shirley (Wiley, New York, 1986) and R.B. Firestone, L.P. Ekstrom, in *Table of Radioactive Isotopes*, Version 2.1 (2004) <http://ie.lbl.gov/toi/index.asp>.
38. J. Blachot, C. Fiche, Ann. Phys. Suppl. **6**, 3 (1981).
39. S. Agostinelli *et al.*, Nucl. Instrum. Methods A **506**, 250 (2005).
40. J. Allison *et al.*, IEEE Trans. Nucl. Sci. **53**, 270 (2006).
41. B. Veyssiere, H. Beil, R. Bergere, P. Carlos, A. Lepretre, Nucl. Phys. A **159**, 561 (1970).
42. C. Fultz, R.L. Bramblett, J.T. Caldwell, N.A. Kerr, Phys. Rev. **127**, 1273 (1962).
43. K. Vogt, P. Mohr, M. Babilon, W. Bayer, D. Galaviz, T. Hartmann, C. Hutter, T. Rauscher, K. Sonnabend, S. Volz, A. Zilges, Nucl. Phys. A **707**, 241 (2002).
44. K.Y. Hara, H. Harada, F. Kitatani, S. Goko, S.Ya. Hohara, T. Kaihori, A. Makinaga, H. Utsunomiya, H. Toyokawa, K. Yamada, J. Nucl. Sci. Tech. **44**, 938 (2007).
45. V.V. Varlamov, B.S. Ishkhanov, V.N. Orlin, S.Yu. Troshchiev, Izv. Rossiiskoi Akad. Nauk, Ser. Fiz. **74**, 884 (2010).
46. V.Di. Napoli, A.M. Lacerenja, F. Salvetti, H.G. De Carvalho, J. Benuzzi Martins, Lett. Nuovo Cimento **1**, 835 (1971).
47. O.A. Bezshyyko, A.N. Vodin, L.O. Golinka-Bezshyyko, A.M. Dovbnaya, I.N. Kadenko, A.O. Kivernyk, A.A. Kovalenko, V.A. Kushnir, A.I. Levon, V.V. Mitrochenko, S.M. Olejnik, G.E. Tuller, Bull. Russ. Acad. Sci. Phys. **75**, 941 (2011).